Electronic Supplementary Material (ESI) for Physical Chemistry Chemical Physics.

Supporting Information for

Formation and Stability of Gas-phase *o*-Benzoquinone from Oxidation of *ortho*-Hydroxyphenyl: A Combined Neutral and Distonic Radical Study

Matthew B. Prendergast,[1] Benjamin B. Kirk,[2] John D. Savee,[3] David L. Osborn,[3] Craig A. Taatjes,[3] Kye-Simeon Masters,[4] Stephen J. Blanksby,[5] Gabriel da Silva,[6] and Adam J. Trevitt[1]*

1. *School of Chemistry, University of Wollongong, Wollongong NSW 2522, Australia.*
2. *Lawrence Berkeley National Laboratory, Berkeley CA 94720, USA*
3. *Combustion Research Facility, Sandia National Laboratories, Livermore CA 94551-0969, USA.*
4. *School of Chemistry, Physics and Mechanical Engineering, Faculty of Science and Engineering, Queensland University of Technology, Brisbane QLD 4001, Australia.*
5. *Central Analytical Research Facility, Queensland University of Technology, Brisbane QLD 4001, Australia.*
6. *Department of Chemical and Biomolecular Engineering, The University of Melbourne, Melbourne VIC 3010, Australia*

Email: adamt@uow.edu.au

1. Synthesis of 4-hydroxy-3-iodo-*N*,*N*,*N*-trimethylbenzenaminium iodide

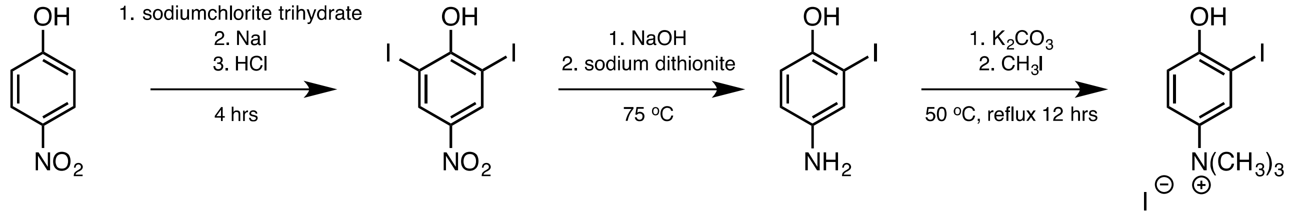

1) 2,6-Diiodo-4-nitrophenol. (Method from Ref. 1)

To a stirred solution of sodiumchlorite trihydrate (11.6 g, 80 mmol) and NaI (23.9 g, 160 mmol) in water (500 mL) was added 4-nitrophenol (5.56 g, 40 mmol) in methanol (500 mL) followed by HCl (11.7 M, 100 mL). After 4 hours the reaction mixture was poured into water (1000 mL) and then extracted with ethyl acetate until the yellow colouration was mostly gone (3-4 x 200 mL). The organics were washed with a saturated aqueous sodium chloride (100 mL) containing sodium thiosulfate (1.0 g), then dried over sodium sulfate. The volatiles were removed on the rotary evaporator (to 30 mBar) to give a yellow-brown solid, 14.1 g, 90% yield. **^{1}H-NMR** (400 MHz, $CDCl_3$): δ 8.65 (s, 2H); The spectral characteristics were in accordance with those reported in the literature.

2) 4-Amino-2-Iodophenol. (Method from Ref. 2)

To a vigorously-stirred suspension of 2,6-diiodo-4-nitrophenol (13.0 g, 33.3 mmol) in $NaOH_{(aq.)}$ (25%, 250 mL), was added sodium dithionite (187 g, 1.07 mol) and the reaction mixture stirred and heated to 75 °C, at which temperature the yellow colouration quickly dissipated. The suspension was then cooled to ambient temperature and quenched with water (500 mL). Repeated extraction of the aqueous phase with ethyl acetate (5 × 250 mL) gave an organic phase that was washed with water (3 x 200 mL) then saturated aqueous sodium chloride (100 mL) and dried over sodium sulfate. The volatiles were removed on the rotary evaporator (to 30 mBar) to give a viscous brown oil. The viscous brown oil was purified by column chromatography on SiO_2 (Grace), with hexanes/ethyl acetate (4:1;

careful elution was required to ensure separation from 2,6-diiodo-4-aminophenol, which was a significant by-product), yielding the title compound as a beige solid (4.31 g).

^{1}H-NMR (400 MHz, d_6-DMSO): δ 9.08 (s, 1H), 6.91 (d, *J* = 2.4 Hz, 1H), 6.57 (d, *J* = 8.3 Hz, 1H), 6.42 (dd, *J* = 8.3, 2.4 Hz, 1H), 4.59 (broad s, 2H). The spectral characteristics were in accordance with those reported in the literature.

3) 4-Hydroxy-3-iodo-N,N,N-trimethylbenzenaminium iodide (Adapted from the Ref. 3)

To a reaction vial was added 4-amino-2-iodophenol (141 mg, 0.60 mmol), anhydrous K_2CO_3 (85 mg, 0.62 mmol) and dry MeOH (5.0 mL). Methyl iodide (370 μL, 6.0 mmol) was added and the vial capped and stirred at 50 °C for 12 hours. The solvent was then removed on the rotary evaporator (to 30 mBar) to yield a dark brown sticky solid. The crude material was dissolved in hot acetonitrile, filtered, and then precipitated by addition of a greater volume of diethyl ether. The precipitate was filtered, washed with a minimal amount of diethyl ether and air dried to yield a dark-grey powder. This material contained a small amount of the anisole derivative, which could be removed by chromatography of this crude material (silica gel, MeOH) to give a beige powder; 141 mg (0.35 mmol, 58 % yield).

^{1}H-NMR (400 MHz, D_2O): δ 8.15 (d, J = 1.2 Hz, 1H), 7.54 (d, J = 9.2 Hz, 1H), 6.88 (dd, J = 9.2, 1.2 Hz, 1H), 3.45 (s, 1H), 3.43 (s, 9H); **^{13}C-NMR** (400 MHz, D_2O): δ 157.0 (C), 139.3 (C), 130.7 (CH), 121.3 (CH), 115.1 (CH), 83.9 (C), 57.1 (CH_3); **LRMS** (ESI+) *m/z* = 278 $[M - I]^+$; **HRMS** (ESI+) m/z for $C_9H_{13}INO^+$ $[M - I]^+$ Calculated: 278.0036; Observed: 278.0032.

2. Supporting Information for Synchrotron photoionisation mass spectrometry: *o*-Hydroxyphenyl + O_2

The multiplexed photoionisation mass spectrometer is comprised of a reactor flow tube, quasi-continuous vacuum-ultraviolet (VUV) synchrotron light source and an orthogonal time-of-flight mass spectrometer. The *o*-hydroxyphenyl + O_2 radical reaction was initiated within the flow tube by photolysis of *o*-bromophenol in the presence of O_2 using a pulsed KrF excimer laser (248 nm) operating at 4 Hz with a fluence of ~50 mJ/cm^2. Gas flow velocities within the reactor were as follows: 10.1 m s^{-1} at 373 K, 13.5 m s^{-1} at 500 K, and 16.2 m s^{-1} at 600 K. And, the total gas flow densities were: 1.0×10^{17} molecule cm^{-3} at 373 K, 7.7×10^{16} molecule cm^{-3} at 500 K, and 6.4×10^{16} molecule cm^{-3} at 600 K.

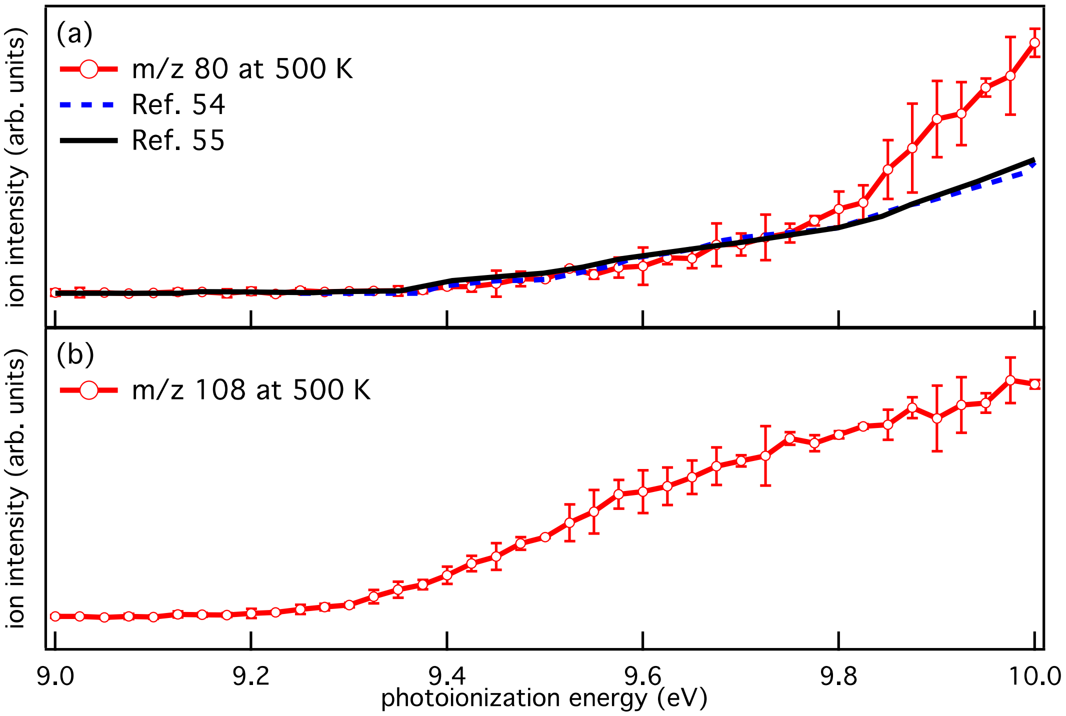

Figure S1. Photoionisation spectra integrated 0–15 ms after 248 nm photolysis for (*a*) *m/z* 80 and (b) *m/z* 108 from the *o*-hydroxyphenyl + O_2 reaction at 500 K. Each spectrum is an average of three PI spectra and the 2σ statistical uncertainty is represented by vertical error bars. Reference PI spectra are provided in (a) for CPO from Ref. 4 and Ref. 5 (873 K) [Ref. 54 and 55, respectively, in the main document].

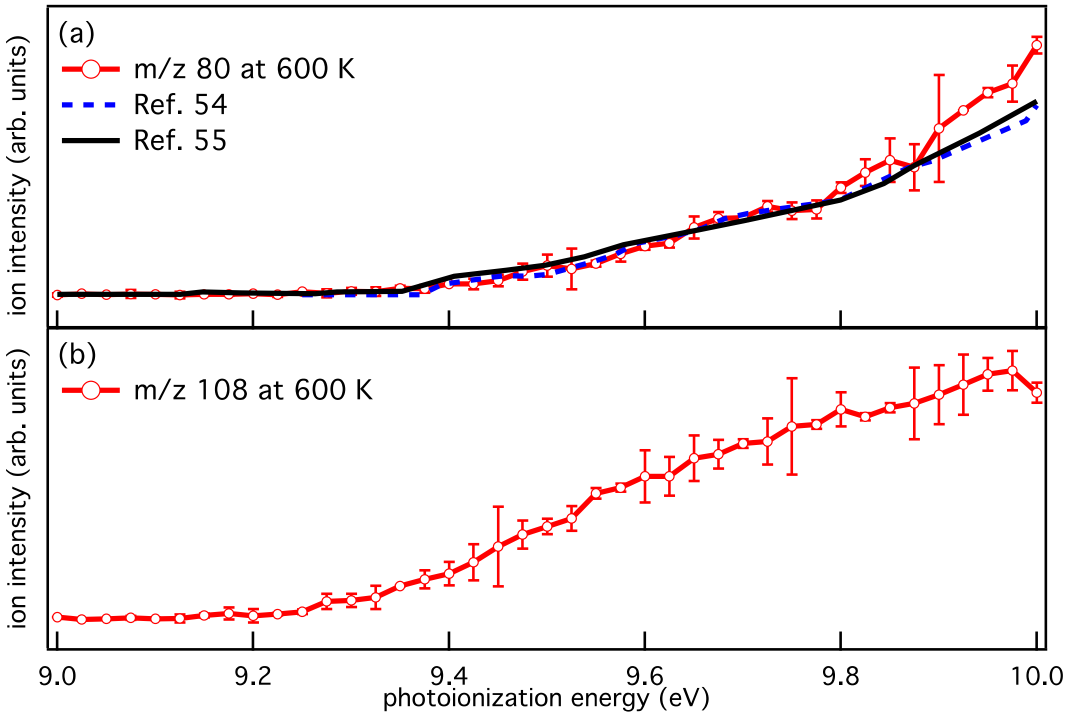

Figure S2. Photoionisation spectra integrated 0–13 ms after 248 nm photolysis for (*a*) *m/z* 80 and (b) *m/z* 108 from the *o*-hydroxyphenyl + O_2 reaction at 600 K. Each spectrum is an average of two PI spectra and the 2σ statistical uncertainty is represented by vertical error bars. Reference PI spectra are provided in (a) for CPO from Ref. 4 and Ref. 5 (873 K) [Ref. 54 and 55, respectively, in the main document].

Table S1. Calculated CBS-QB3 adiabatic ionisation energies for linear C_5H_4O isomers (*m/z* 80). None of the C_5H_4O isomers listed have a calculated adiabatic ionisation energy of 9.8 eV. G3XK enthalpies (ΔH_f) provided in kcal mol^{-1} with zero-point energy.

C_5H_4O isomer	Adiabatic Ionisation Energies CBS-QB3 (eV)	Literature Ionisation Energies (eV)	Relative ΔH_f (kcal mol^{-1})
Cyclopentadienone (CPO)	9.4		0
penta-1,4-diyn-3-ol	10.4		60.2
penta-1,2-dien-4-yn-3-ol	8.7		
pentatetraen-1-ol	8.2		
pent-2-en-4-ynal	10.0		27.7
pent-1-en-4-yn-3-one	10.1		29.0
penta-1,2,4-trien-1-one	8.8		
penta-1,3,4-trien-1-one (allenylketene)	8.2	8.12 [6]	
pent-1-en-3-yn-1-one (propynylketene)	8.4	8.25 [6]	
pent-1-en-4-yn-1-one	9.0		

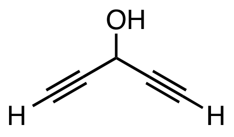

penta-1,4-diyn-3-ol

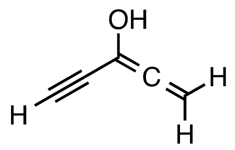

penta-1,2-dien-4-yn-3-ol

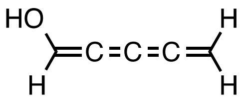

pentatetraen-1-ol

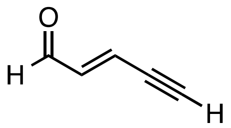

pent-2-en-4-ynal

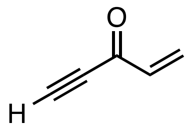

pent-1-en-4-yn-3-one

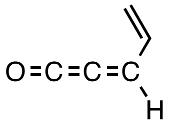

penta-1,2,4-trien-1-one

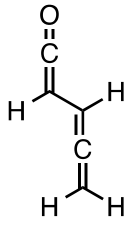

penta-1,3,4-trien-1-one
(allenylketene)

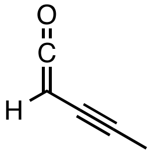

pent-1-en-3-yn-1-one
(propynylketene)

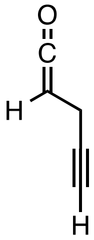

pent-1-en-4-yn-1-one

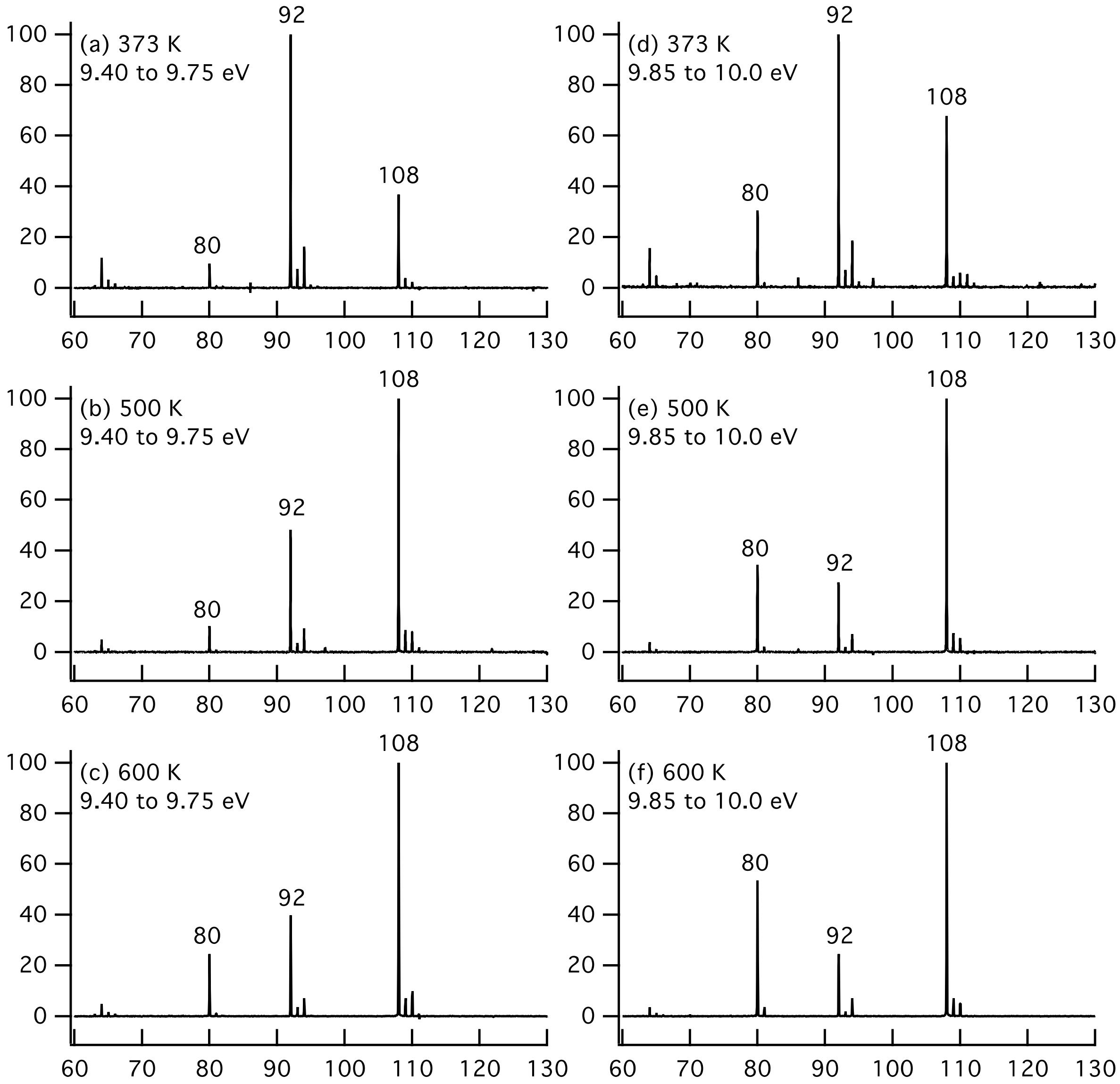

Figure S3. Product mass spectra for *o*-hydroxyphenyl radical + O_2 reaction integrated from 9.4 to 9.75 eV (*left panel: a, b, and c*) and 9.85 to 10 eV (*right: d, e, and f*) at 373 K (*a and d*) 0–20 ms, 500 K (*b and e*) 0–15 ms, and 600 K (*c and f*) 0–13 ms after photolysis.

The kinetic traces in Figure S4 show the ion signal rapidly rise following the photolysis laser pulse at ca. 20 ms and thus, demonstrates the laser dependency of radical generation. As the temperature of the reactor is raised, because the pressure and gas delivery parameters are held constant, the volumetric flow rate increases while the number density decreases. This manifests in faster reactor pump-out times as indicated by ion signals rapidly dropping at about 50 ms at 500 K (Figure S4).

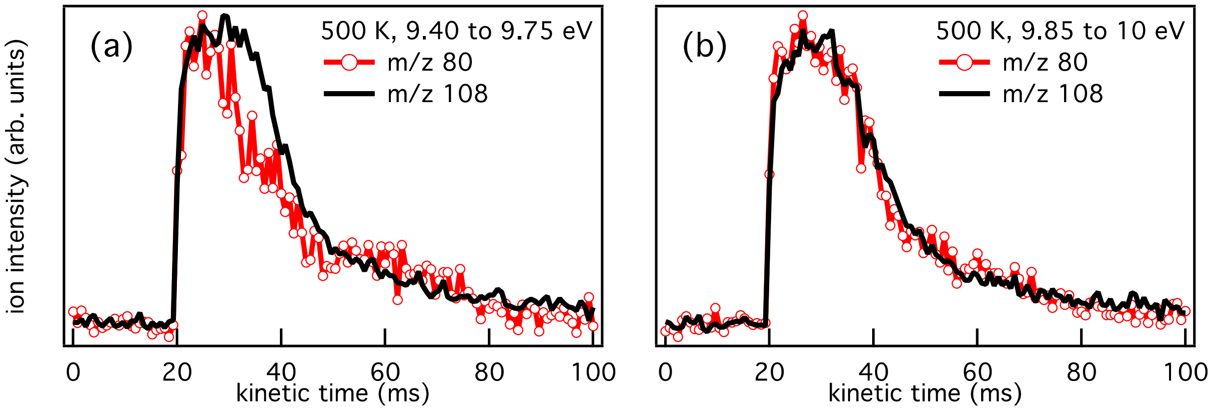

Figure S4. Kinetic traces of the ion signal at *m/z* 80 (*red with empty circles*) and *m/z* 108 (*black*) for the *o*-hydroxyphenyl + O_2 reaction integrated (a) from 9.4 to 9.75 eV and (b) from 9.85 to 10 eV 500 K. Gas flow velocity was 13.5 m s^{-1} and the total gas flow density was 7.7×10^{16} molecule cm^{-3} at 500 K.

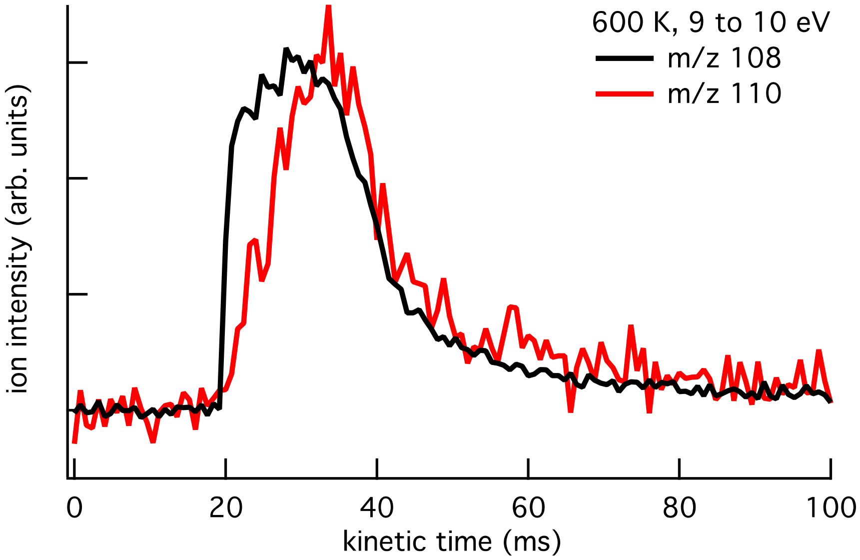

Figure S5. Kinetic traces of the ion signal at *m/z* 108 (*red*) and *m/z* 110 (*black*) from the *o*-hydroxyphenyl + O_2 reaction integrated 9.0 to 10.0 eV at 600 K. The gas flow velocity was 16.2 m s^{-1} and the total gas flow density was 6.4×10^{16} molecule cm^{-3} at 600 K.

3. Supporting Information for Ion-trap Mass Spectrometry: Distonic *o*-Hydroxyphenyl + O_2

Radical precursor ions were generated by infusing methanolic solutions of ca. 10 μM of 3-bromo-4-methylaniline ($[M + H]^+$ at *m/z* 186 and 188) or 3-iodo-4-hydroxy-*N*,*N*,*N*-trimethylbenzenaminium iodide ($[M + H]^+$ at *m/z* 278) into the electrospray ion source at 5 μL min^{-1}. The resulting cations were mass-selected using an isolation window of 5–6 Th for brominated, and 1-2 Th for the iodinated cations with a q-factor of 0.250.

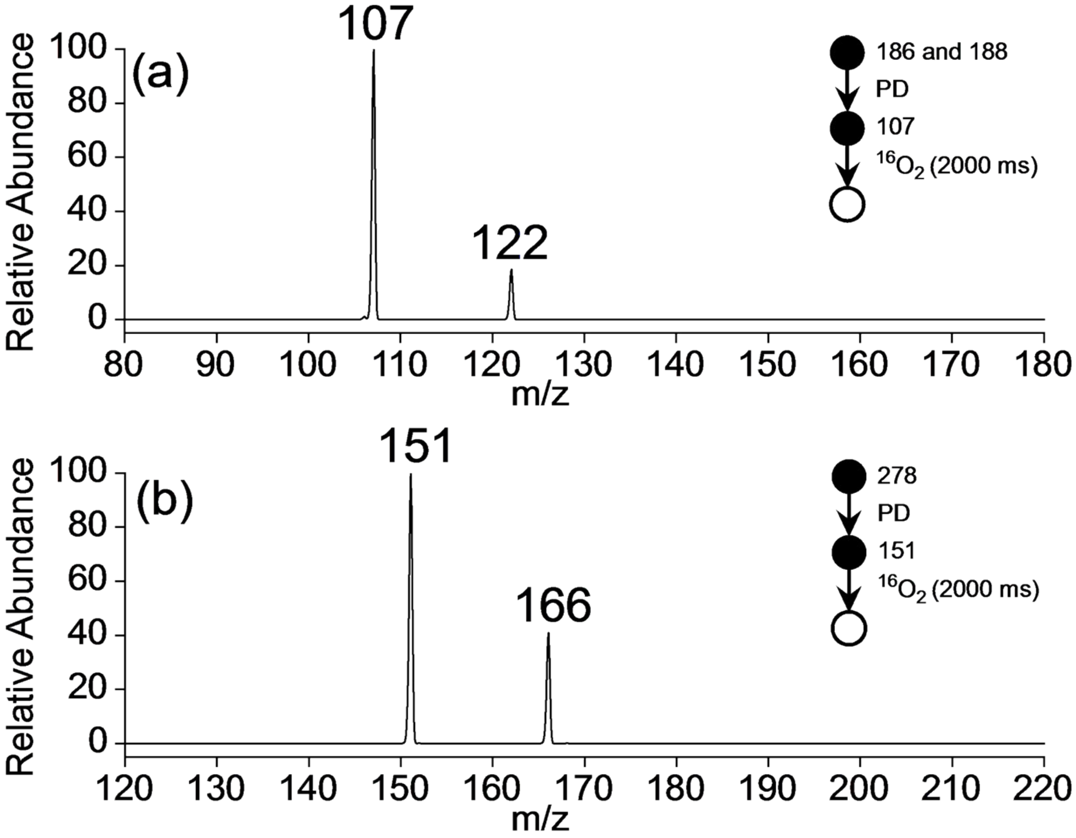

Figure S6. Mass spectrum (a) is produced by PD of 3-bromo-4-methylbenzenaminium (*m/z* 186 and 188) and isolation of the resulting *m/z* 107 ion in the presence of background O_2 ($[O_2] = 6.4 \pm 0.4 \times 10^9$ molecules cm^{-3}) for 2000 ms and (b) by PD of 3-iodo-4-hydroxy-*N*,*N*,*N*-trimethylbenzenaminium cations (*m/z* 278) and isolation of the resulting *m/z* 151 ion in background O_2 ($[O_2] = 6.6 \pm 0.3 \times 10^9$ molecules cm^{-3}) for 2000 ms.

Equation (1) was fitted to experimental data (e.g. Figure S7 and S8) for decay of *m/z* 107 and 151 radical cations by reactions with O_2. Experimental data was found to be consistent with pseudo-first order kinetic behaviour. Residuals from the fitting of Equation 1 also are provided in Figure S5 and S6 above the respective kinetic plots. The second-order rate coefficient (k_{2nd}) for *m/z* 151 and 107 radical cation decay are provided in Table 2 in the main document.

Equation 1 is repeated here for the reader:

$$y = A_0 \exp(-k_{1st}t) + \text{constant} \qquad (1)$$

Where A_0 is the pre-exponential factor, k_{1st} is the exponential decay coefficient, and the constant term presents the vertical-offset.

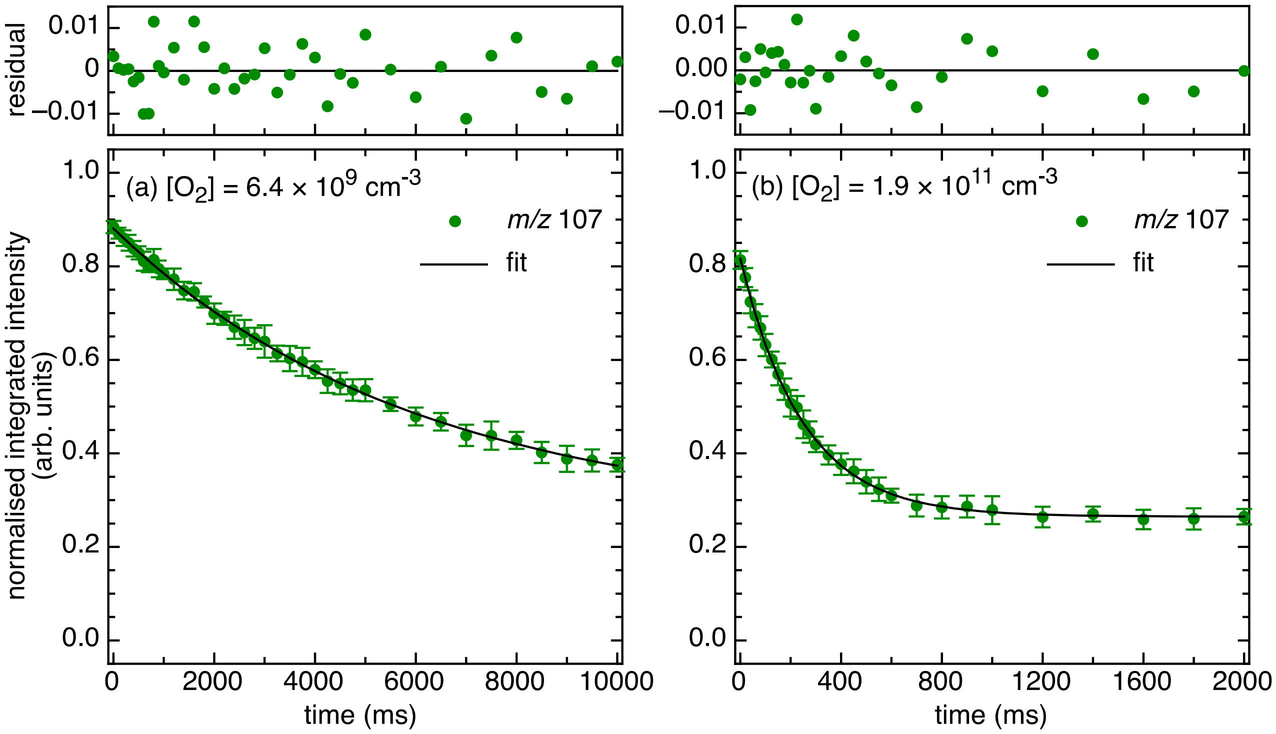

Figure S7. Example kinetic curves for *m/z* 107 (solid green circles), from PD of 3-bromo-4-methylbenzaminium cation, from reactions with (a) background O_2 (6.4×10^9 molecules cm^{-3}) and (b) increased O_2 (1.9×10^{11} molecules cm^{-3}). Residual plots from the fitting of Equation (1) is provided above.

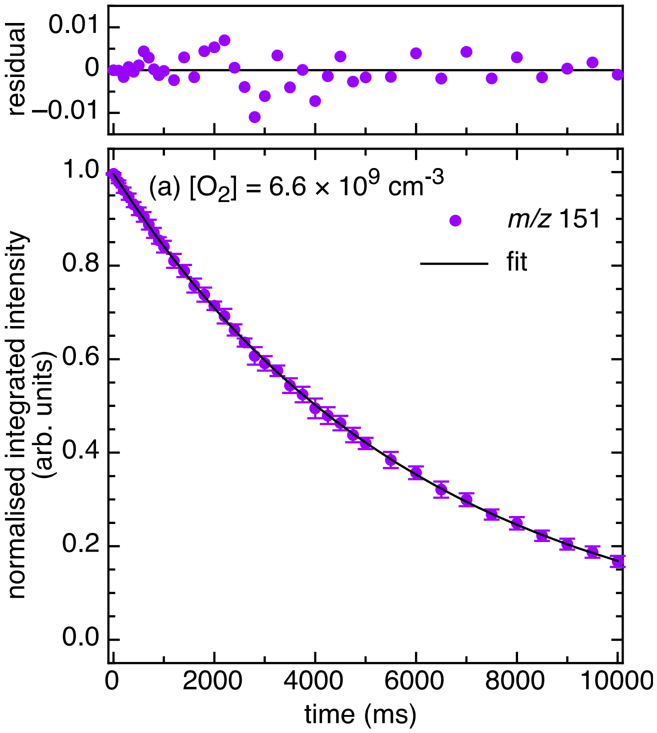

Figure S8. An example kinetic curves for *m/z* 151 (solid purple circles), from PD of 3-iodo-4-hydroxy-*N*,*N*,*N*-trimethylbenzenaminium cations, reactions with background O_2 (6.6 × 10^9 $\text{cm}^{=3}$). A residual plot from the fitting of Equation (1) is provided above.

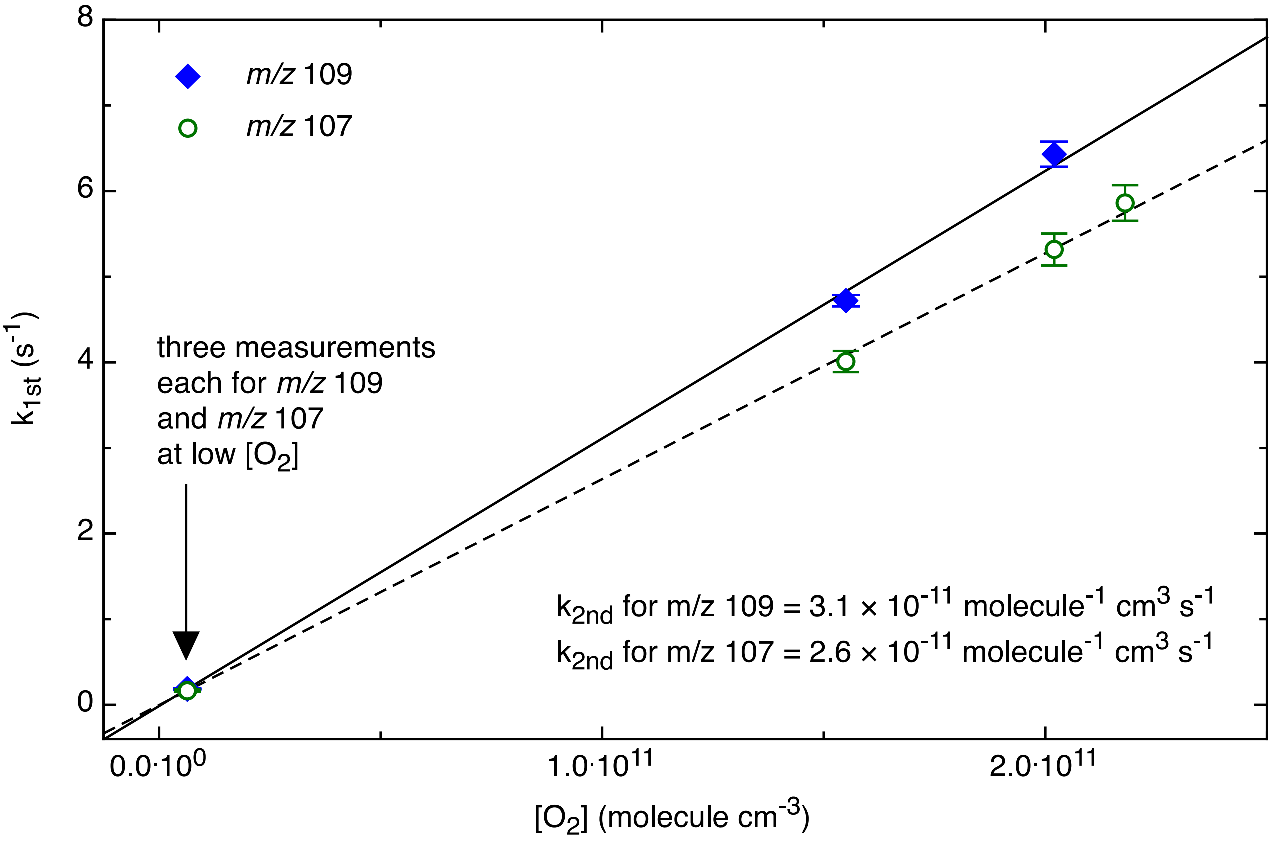

Figure S9. A plot of the measured pseudo-first order rate coefficients (k_{1st}) versus measured [O_2] for *m/z* 109 ions (solid blue circles), from PD of 3-bromo-4-hydroxybenzaminium cations, and *m/z* 107 (green circles), from PD of 3-bromo-4-methylbenzaminium cations. The error bars in k_{1st} are 2σ and the linear regression uses 50% uncertainty for [O_2]. The slope of the fitted lines for *m/z* 109 (solid) and *m/z* 107 (dashed) are in accord with reported k_{2nd} in Table 2 in the main document.

4. Supporting Information for Computational Chemistry and Reaction Mechanism

To determine whether a through-space effect from the positively charged ammonium could account for the 13.0 kcal mol^{-1} difference in reaction enthalpy shown in Figure 6 (main document) we employed an approach undertaken by Grob et al.[7] and used again more recently[8, 9] for understanding the effect of a change tag on a property of interest. In this investigation the reaction enthalpies for a series of H_3N^+-$(CH_2)_n$-tagged *o*-hydroxyperoxyl → *o*-BQ + OH reactions were calculated using the M06-2X/6-311++G(d,p) method, where the number methylene links (n = 0 to 7) was increased in a zig-zag configuration to progressively separate the ammonium tags from the ring structures. The dihedral angle between the H_3N^+-$(CH_2)_n$ substituent and the *o*-hydroxyphenylperoxyl, and *o*-BQ ring structures was maintain at ~90°. Charge separation (r) was measured between the ammonium-nitrogen and hydroxy-oxygen of the respective H_3N^+-$(CH_2)_n$-tagged *o*-hydroxyphenylperoxyl radical. The reaction enthalpies plotted in Figure S10 decrease linearly with 1/r and approach the reaction enthalpy for neutral *o*-hydroxyperoxyl → *o*-BQ (-0.9 kcal mol^{-1}), as can be expected for though-space charge effects. The reported 0 K enthalpies in Figure S10 were calculated using the M06-2X/6-311++G(d,p) method and include the zero-point energy correction.

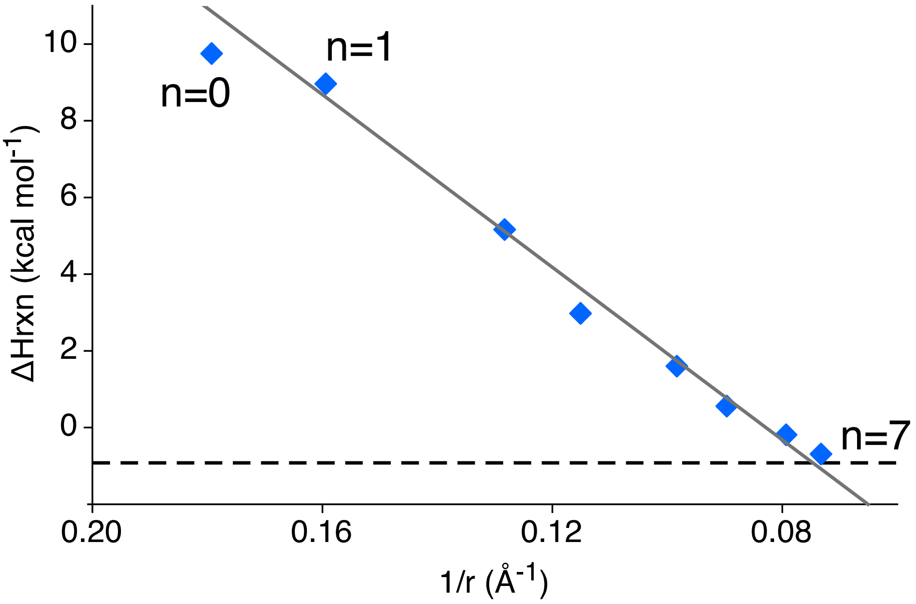

Figure S10. Reaction enthalpies (0 K) for H_3N^+-$(CH_2)_n$ tagged *o*-hydroxyphenylperoxyl (**C2**) → *o*-BQ + OH reduced linearly as a function of 1/r and converged toward that for the corresponding neutral reaction (-0.9 kcal mol^{-1}). When n = 7, the difference is ~0.2 kcal mol^{-1}. Structures were calculated using the M06-2X/6-311++G(d,p) method and are reported in kcal mol^{-1} relative to the H_3N^+-$(CH_2)_n$-$C_6H_3(OH)OO^\bullet$ homologue series.

The **N4→N5→N6→N8** CO elimination mechanism in Figure 7 (main document) was applied to the ammonium-tagged *o*-BQ decomposition as **C4→C5→C6a→C8** and **C4→C5→C6b→C8** as shown Figure S11. These mechanisms feature barriers that exceed the energy of 5-ammonium-2-hydroxyphenyl + O_2 by 2.8 kcal mol^{-1} via **TS C6a** → **C8** and 6.7 kcal mol^{-1} via **TS C6b** → **C8**. When the alternate mechanism in Figure 7 (i.e. via **N7**) is applied to the distonic system, greater differences between the neutral and distonic systems emerge. A mechanism was found that connects via **TS C5** → **C7** without transmitting through the **C6a** or **C6b** intermediates. Also, CO may eliminate from the **C5** to produce the ammonium-tagged CPO (*m/z* 96). The reaction barrier for the last two mechanisms is 35.0 kcal mol^{-1} (3.8 kcal mol^{-1} below 5-ammonium-2-hydroxyphenyl + O_2).

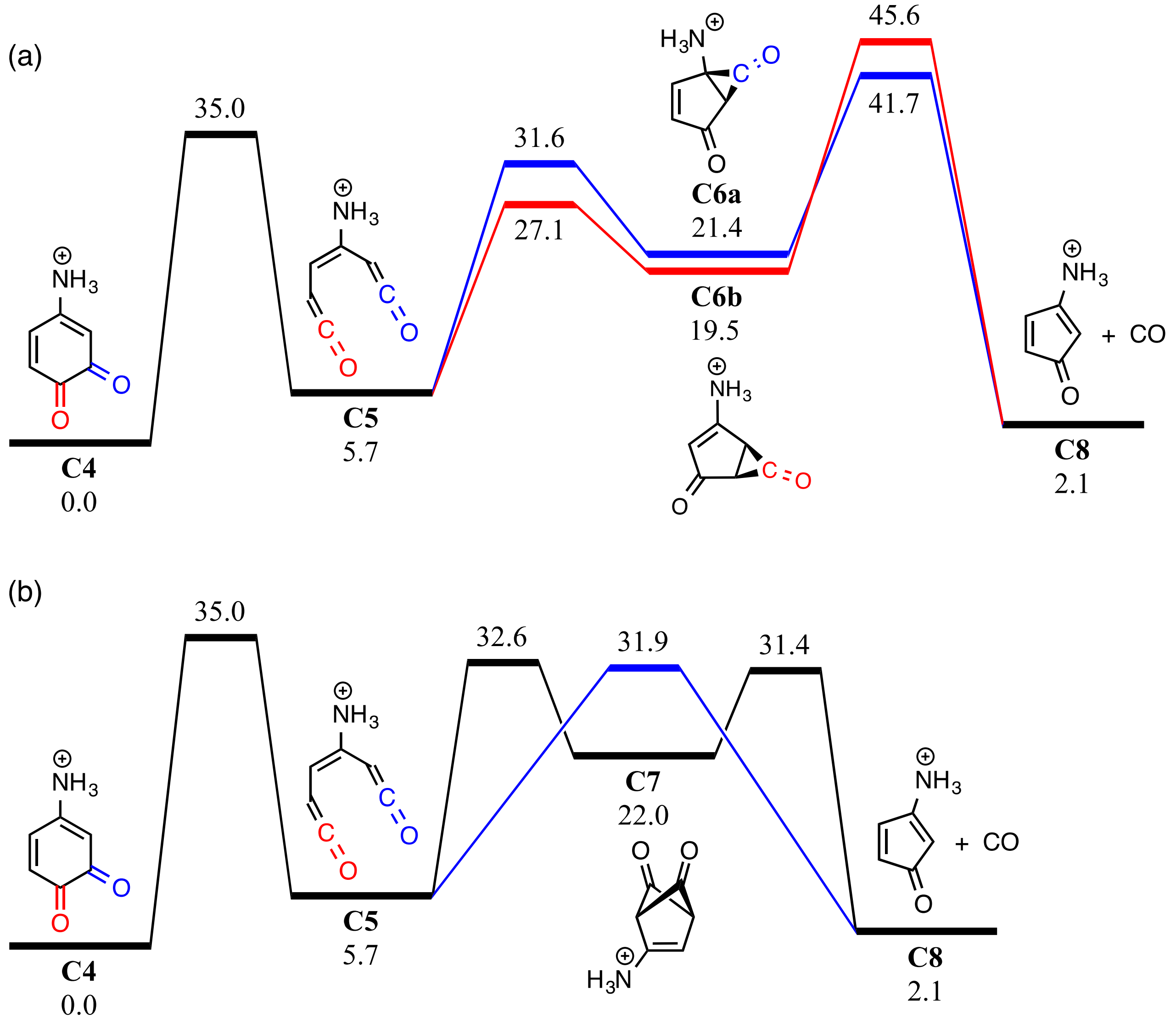

Figure S11. Potential energy schematics for (a) CO elimination mechanism proposed by Shokov *et al* (Ref. 10) as applied to the ammonium-tagged *o*-BQ and (b) additional pathways that also result in tagged CPO + CO. Coloured pathways indicate which of the two carbonyl groups in *o*-BQ is eliminated: Red for the para-carbonyl and blue for the meta-carbonyl group. G3X-K energies are reported in kcal mol^{-1} relative to 4-ammonium-2-benzoquinone.

Figure S12 shows the formation of the *o*-hydroxyphenoxyl radical via O(^{3}P) elimination and subsequent CO loss to generate CPO. Elimination of O(^{3}P) from *o*-hydroxyphenylperoxyl requires 30.6 kcal mol^{-1} to produce OH-*cis* *o*-hydroxyphenoxyl and 39.3 kcal mol^{-1} for OH-*trans* *o*-hydroxyphenoxyl radicals (a difference of 8.7 kcal mol^{-1}). The loss of CO from *o*-hydroxyphenoxyl results in a OH-substituted cyclopentadienyl radical[11] that eliminates the hydroxy-H atom to produce CPO.[12] The reaction barrier to CPO + H + CO + O(^{3}P), via *o*-hydroxyphenoxyl, exceeds the energy of *o*-hydroxyphenyl + O_2 by 61.1 kcal mol^{-1}. Within the corresponding distonic radical ion scheme, reactions leading to OH-*cis* ammonium-tagged *o*-hydroxyphenoxyl proceed with a 32.0 kcal mol^{-1}

barrier (7.5 kcal mol^{-1} below the corresponding OH-*trans* barrier) and with a overall reaction barrier 69.9 kcal mol^{-1} above the distonic *o*-hydroxyphenyl + O_2 reactants. These high barriers may be surmounted at high temperatures, e.g. in combustion, however, may be prohibitive under the experimental conditions reported here without additional activation.

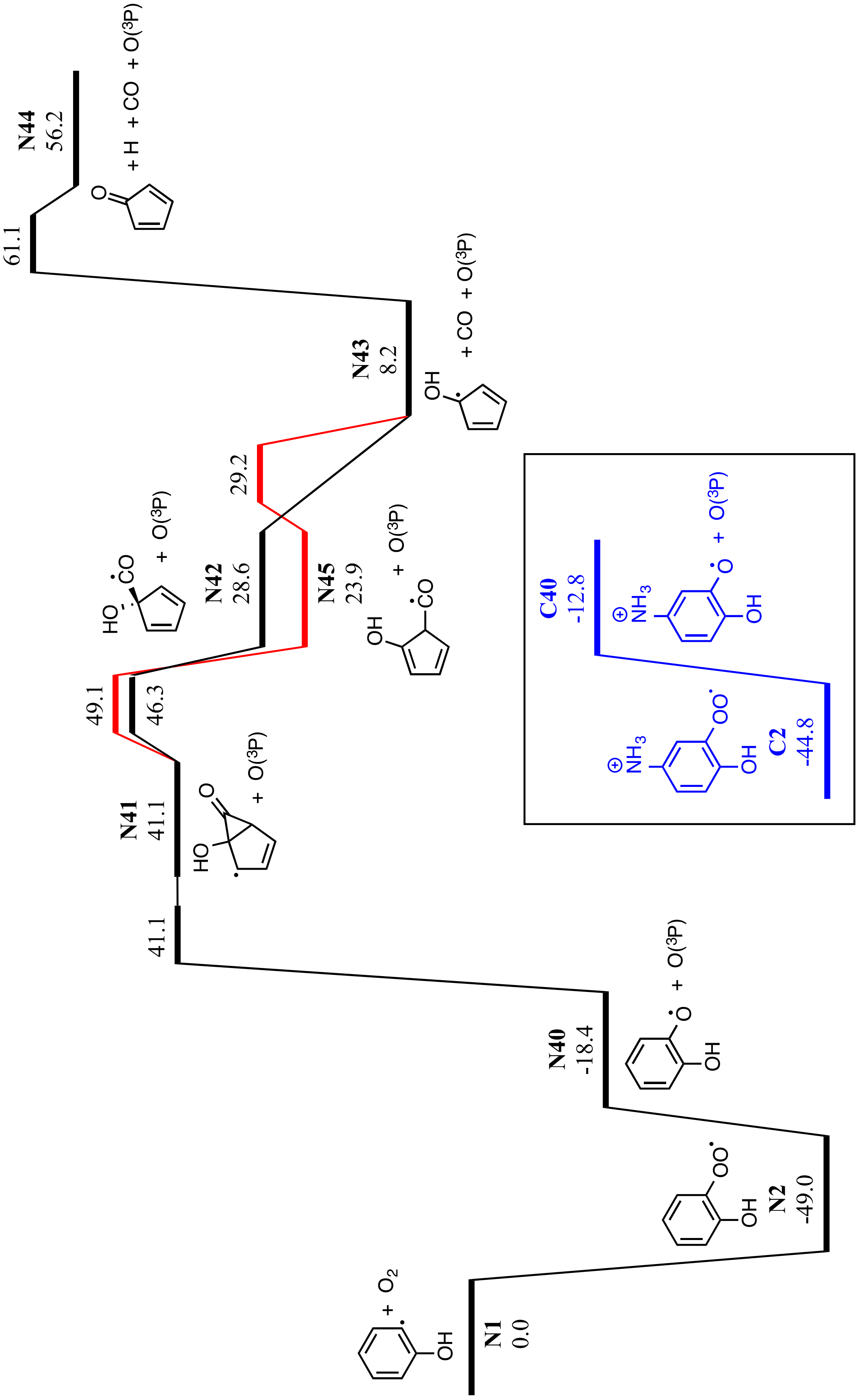

Figure S12. Potential energy schematic for O(^{3}P) and subsequent CO loss from *o*-hydroxyphenoxyl, followed by H-atom elimination to generate the CPO + H + CO + O(^{3}P) product (**N44**). The corresponding O(^{3}P) loss on the charge-tagged reaction surface is provided as an inset. Energies were calculated using the G3X-K composite method and reported in kcal mol^{-1} relative to the respective *o*-hydroxyphenyl + O_2.

Figure 8 (main document) shows the potential energy schematic for reactions of *o*-hydroxyphenylperoxyl (**N2**) toward 7-hydroxyoxepinoxyl (**N23**) and 6-carboxy-1-oxo-hex-2,4-dienyl radicals (**N21**) via dioxirane-hydroxycyclohexadienyl intermediates. Formation of the 6-carboxy-1-oxo-hex-2,4-dienyl radical (**N21**) is initiated via **TS N2 → N20** with a barrier 11.6 kcal mol^{-1} above **TS N3 → N4** (Figure 6 in the main document). Projection of imaginary frequency normal modes for succeeding **TS3n** and **TS4n** reveal another possible first-order saddle point on the reaction surface. The **TS2n** IRC was calculated and was found to proceed through a 1,4-H atom shift and C-C bond cleavage to produce 6-carboxy-1-oxo-hex-2,4-dienyl with 97.1 kcal mol^{-1} activation.

Reactions toward 7-hydroxyoxepinoxyl proceed through the rate limiting **TS N2 → N22** with a 27.7 kcal mol^{-1} barrier. This transition state exceeds the rate limiting step toward *o*-BQ by 18.1 kcal mol^{-1} at 0 K. Cleavage of the O-O bond in **N22** through **TS3n** is accompanied by O-atom ring insertion (**TS4n**) to produce 7-hydroxyoxepinyl with 102.3 kcal mol^{-1} activation. By analogy to *o*-methyphenyl + O_2,[13] both 3-hydroxyoxepinoxyl and 7-hydroxyoxepinoxyl radicals are expected after bifurcation[14] of the reaction surface after **TS3n**. However, projection of the imaginary frequency normal mode in **TS3n** and the subsequent **TS4n** suggest the presence of a first-order saddle point at **TS4n** that exceeds **TS3n** in energy with ZPE correction and not a point for bifurcation.

Reaction processes of the charged-tagged *o*-hydroxphenylperoxyl toward hydroxyoxepinoxyl and 6-carboxyoxohexdienyl radicals in Figure S13 generally parallel those described by Figure 8 for the neutral reaction scheme. The sequential **TS3c** (-5.2 kcal mol^{-1}) and **TS4c** (30.7 kcal mol^{-1}), succeeding the OH-*trans* dioxiranyl intermediate (**C22**), represent a bifurcation of the potential energy surface toward the 4-ammonium-7-hydroxyoxepinoxyl radical (**C23**) and new 6-ammonium-3-hydroxyoxepinoxyl radical (**C24**). In addition, the rate limiting **TS3c** is 22.2 kcal mol^{-1} above **TS C3 → C4** (Figure 6). Production of the ammonium-tagged carboxyoxohexdienyl radical is more competitive then the hydroxyoxepinoxyl intermediate with the rate limiting **TS1c** just 5.1 kcal mol^{-1} greater than **TS C3** → **C4**.

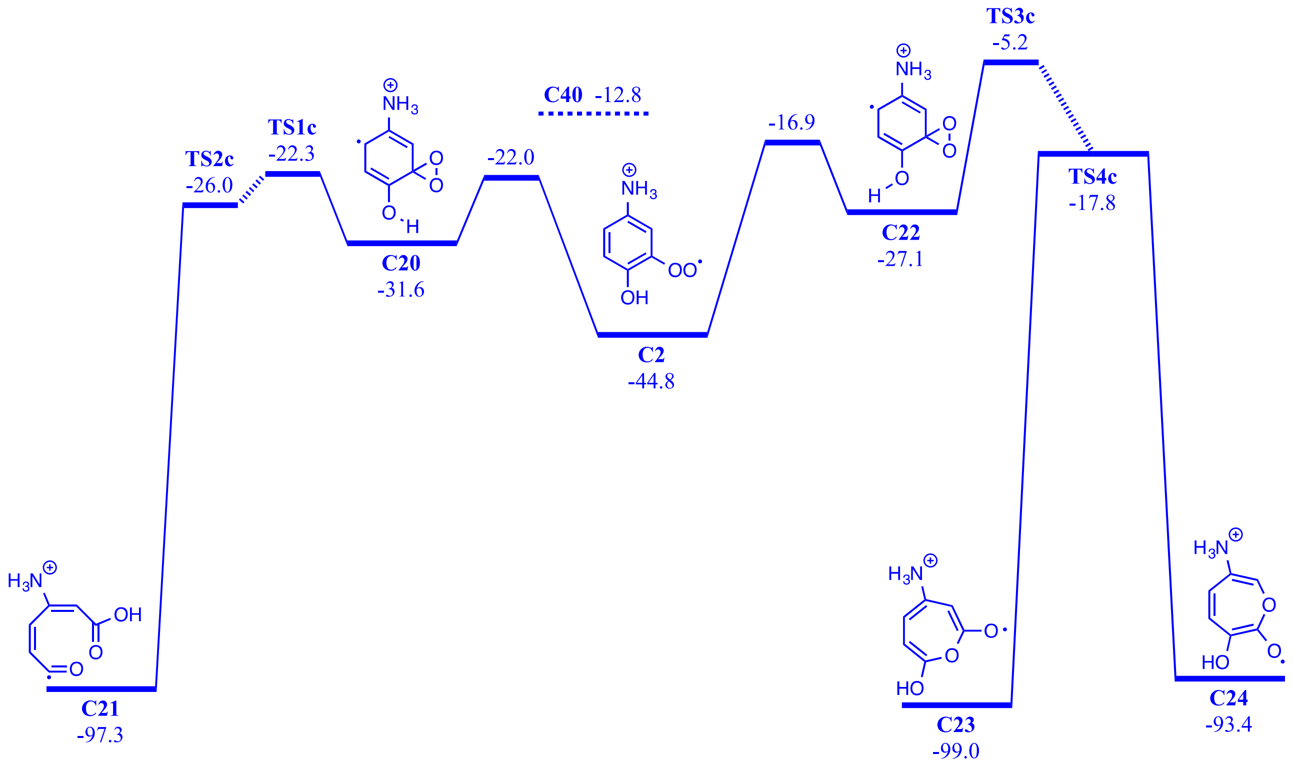

Figure S13. Potential energy schematic comparing the OH-cis and OH-trans reaction pathways to the ammonium-tagged hydroxyoxepinoxyl and 6-carboxy-1-oxo-hex-2,4-dienyl intermediates along the charge-tagged *o*-hydroxyphenyl + O_2 reaction surface. The reaction enthalpy for the tagged *o*-hydroxyphenoxyl radical (**C40**) is also included for comparison. G3X-K energies are reported in kcal mol^{-1} relative to 5-ammonium-2-hydroxyphenyl + O_2.

Informed by Kirk et al.,[3] the 7-hydroxyoxepinoxyl and 3-hydroxyoxepinoxyl radicals can possibly decompose to generate *o*-BQ and CPO, including hydroxy-substituted equivalents via the pathways described in Figure S14 and Figure S15.

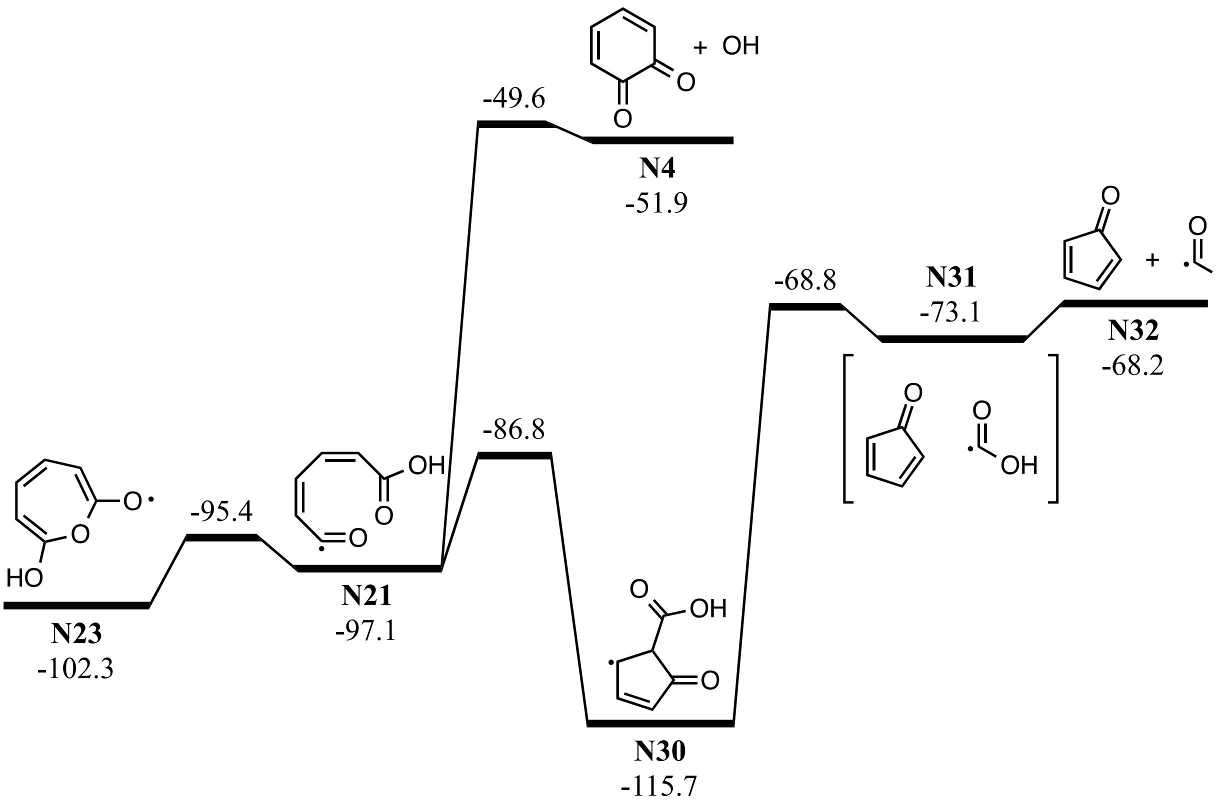

Figure S14. Potential energy schematic showing decomposition pathways for 7-hydroxyoxepinoxyl and 6-carboxy-1-oxo-hex-2,4-dienyl toward *o*-BQ + OH and CPO + HOCO. G3X-K energies are reported in kcal mol^{-1} relative to *o*-hydroxyphenyl + O_2.

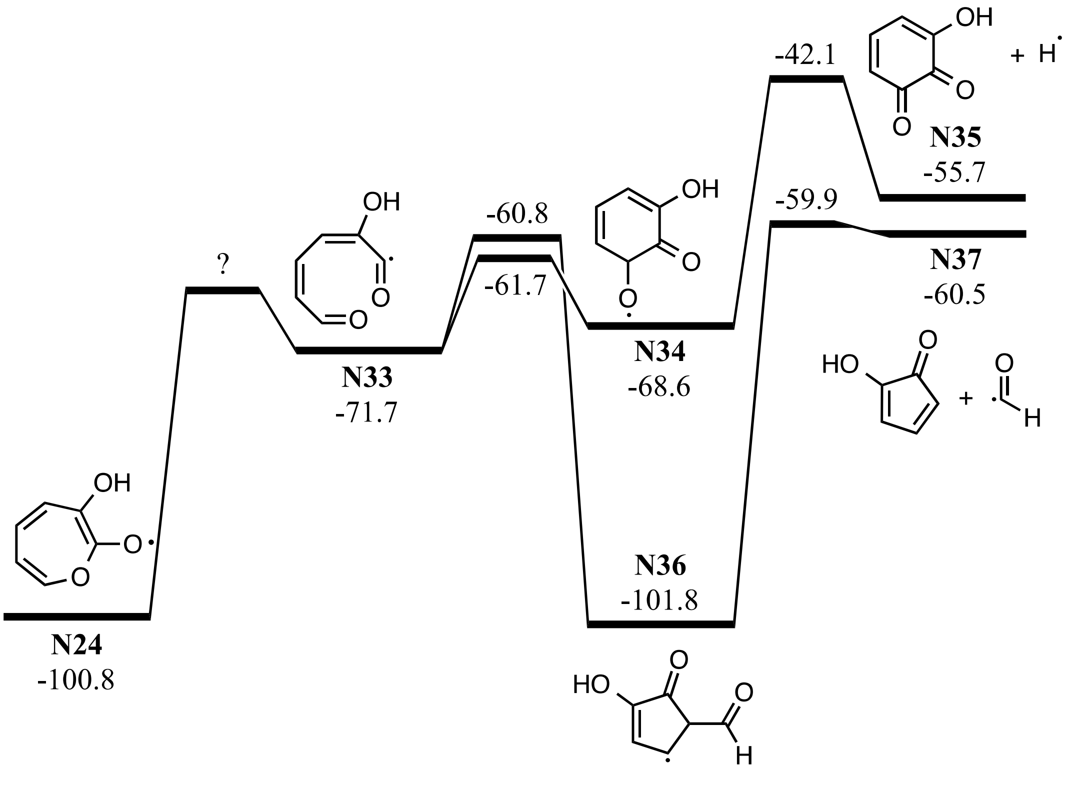

Figure S15. Potential energy schematic showing decomposition pathways for the 3-hydroxyoxepinoxyl radical toward 3-hydroxy-2-benzoquinone + H and 2-hydroxy-cyclopentadienone + HCO. G3X-K energies are reported in kcal mol^{-1} relative to *o*-hydroxyphenyl + O_2.

Table S2. The sum of states for the transition structures (i.e. $N^{\ddagger}(E-E_0)$) and the energy dependent rate coefficient from Equation 2 are provided for salient unimolecular processes from 2-hydroxyphenylperoxyl radical toward o-BQ, hydroxy-oxepinoxyl and carboxyoxohexdienyl radicals.

Reaction Process		$N^{\ddagger}(E-E_0)$	k(E) (s^{-1})
2-hydroxyphenylperoxyl radical (N2)	→ 2-hydroperoxyphenoxyl radical (N3)	5.06×10^{16}	2.73×10^{12}
	→ OH-*cis* dioxiranyl radical (N20)	1.83×10^{13}	9.88×10^{8}
	→ OH-*trans* dioxiranyl radical (N22)	4.70×10^{11}	2.53×10^{7}
2-hydroperoxyphenoxyl radical (N3)	→ o-benzoquinone (N4) + OH	2.97×10^{16}	6.60×10^{11}
	→ 2-hydroxyphenylperoxyl radical (N2)	5.06×10^{16}	1.12×10^{12}
OH-*cis* dioxiranyl radical (N20)	→ 6-carboxyoxohexdienyl radical (N21)	1.23×10^{14}	9.04×10^{11}
	→ 2-hydroxyphenylperoxyl radical (N2)	1.83×10^{13}	1.35×10^{11}
OH-*trans* dioxiranyl radical (N22)	→ 7-hydroxyoxepinoxyl radical (N23)	3.79×10^{12}	3.77×10^{11}
	→ 2-hydroxyphenylperoxyl radical (N2)	4.70×10^{11}	4.66×10^{10}

In Equation 2, k(E) is the rate coefficient for a unimolecular process with the total energy of E, which is taken as the energy of the *o*-hydroxyphenyl + O_2 reactants. The $N^{\ddagger}(E-E_0)$ term is the sum of states for a transition state with the critical energy of E_0 up to the total energy and $\rho(E)$ is the density of states for the reactant intermediate for the total energy.

$$k(E) = \frac{N^{\ddagger}(E-E_0)}{h\,\rho(E)} \qquad (2)$$

REFERENCES

1. L. Lista, A. Pezzella, A. Napolitano and M. d'Ischia, Mild and Efficient Iodination of Aromatic and Heterocyclic Compounds with the Naclo2/Nai/Hcl System, *Tetrahedron*, 2008, **64**, 234-239.
2. K. R. Kunz, B. S. Iyengar, R. T. Dorr, D. S. Alberts and W. A. Remers, Structure Activity Relationship for Mitomycin C and Mitomycin A Analogs, *J. Med. Chem.*, 1991, **34**, 2281-2286.
3. B. B. Kirk, D. G. Harman, H. I. Kenttämaa, A. J. Trevitt and S. J. Blanksby, Isolation and Characterization of Charge-Tagged Phenylperoxyl Radicals in the Gas Phase: Direct Evidence for Products and Pathways in Low Temperature Benzene Oxidation, *Phys. Chem. Chem. Phys.*, 2012, **14**, 16719-16730.
4. J. Yang, Photonionization Cross Section Database, *Center for Advanced Combustion and Energy*, 2011.
5. D. S. N. Parker, R. I. Kaiser, T. P. Troy, O. Kostko, M. Ahmed and A. M. Mebel, Toward the Oxidation of the Phenyl Radical and Prevention of Pah Formation in Combustion Systems, *J. Phys. Chem. A*, 2014 (*in Press*).
6. X. Wu, Z. Huang, T. Yuan, K. Zhang and L. Wei, Identification of Combustion Intermediates in a Low-Pressure Premixed Laminar 2,5-Dimethylfuran/Oxygen/Argon Flame with Tunable Synchrotron Photoionization, *Combust. Flame*, 2009, **156**, 1365-1376.
7. C. A. Grob, A. Kaiser and T. Schweizer, The Transmission of Polar Effects Polar Effects. Part II, *Helv. Chim. Acta*, 1977, **60**, 391-399.
8. G. Gryn'ova, D. L. Marshall, S. J. Blanksby and M. L. Coote, Switching Radical Stability by Ph-Induced Orbital Conversion, *Nat Chem*, 2013, **5**, 474-481.
9. A. T. Maccarone, B. B. Kirk, C. S. Hansen, T. M. Griffiths, S. Olsen, A. J. Trevitt and S. J. Blanksby, Direct Observation of Photodissociation Products from Phenylperoxyl Radicals Isolated in the Gas Phase, *J. Am. Chem. Soc.*, 2013, **135**, 9010–9014.
10. S. Skokov, A. Kazakov and F. L. Dryer, presented in part at the Fourth Joint Meeting of the U.S. Sections of the Combustion Institute, Philadelphia, PA., March 20-23, 2005.
11. H.-H. Carstensen and A. M. Dean, A Quantitative Kinetic Analysis of CO Elimination from Phenoxy Radicals, *Int. J. Chem. Kinet.*, 2012, **44**, 75-89.
12. A. M. Scheer, C. Mukarakate, D. J. Robichaud, M. R. Nimlos and G. B. Ellison, Thermal Decomposition Mechanisms of the Methoxyphenols: Formation of Phenol, Cyclopentadienone, Vinylacetylene, and Acetylene, *J. Phys. Chem. A*, 2011, **115**, 13381-13389.
13. G. da Silva, C.-C. Chen and J. W. Bozzelli, Toluene Combustion: Reaction Paths, Thermochemical Properties, and Kinetic Analysis for the Methylphenyl Radical + O_2 Reaction, *J. Phys. Chem. A*, 2007, **111**, 8663-8676.
14. D. H. Ess, S. E. Wheeler, R. G. Iafe, L. Xu, N. Çelebi-Ölçüm and K. N. Houk, Bifurcations on Potential Energy Surfaces of Organic Reactions, *Angew. Chem. Int. Ed.*, 2008, **47**, 7592-7601.